



Ethanol electro-oxidation activity of Nb-doped-TiO₂ supported PdAg catalysts in alkaline media

Son Truong Nguyen, Yanhui Yang, Xin Wang*

School of Chemical and Biomedical Engineering, Nanyang Technological University, 62 Nanyang Drive, Singapore 637459, Singapore

ARTICLE INFO

Article history:

Received 18 July 2011

Received in revised form 17 October 2011

Accepted 27 November 2011

Available online 6 December 2011

Keywords:

Ethanol oxidation

Palladium-silver

Direct ethanol fuel cell

Nb-doped TiO₂

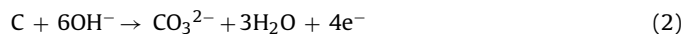
ABSTRACT

Various mesoporous Nb-doped titania materials were synthesized by a hydrothermal method and examined as catalyst support for PdAg alloy particles for alkaline direct ethanol fuel cell (ADEFC). X-ray diffraction, nitrogen adsorption/desorption, transmission electron microscopy (TEM), cyclic voltammetry (CV) and chronoamperometry (CA) were used to investigate the properties of the supports and catalysts. 700 °C was found as the optimal activation temperature for Nb-doped TiO₂ due to the high electronic conductivity achievement and mesoporosity conservation. X-ray diffraction (XRD) revealed that Nb_xTi_{1-x}O₂ had a structure of mixed anatase and rutile phases. PdAg/Nb_xTi_{1-x}O₂ exhibited excellent performance for the electrooxidation of ethanol and higher durability in alkaline solution compared with PdAg/C and PdAg/commercial TiO₂. The results open a new way to develop durable and effective electrocatalysts for ADEFC.

© 2011 Elsevier B.V. All rights reserved.

1. Introduction

Support materials for catalysts play an important role in polymer electrolyte membrane fuel cells (PEMFCs). Major requirements for support material include (1) large surface area for the dispersion and stabilization of catalyst nanoparticles, (2) good electrical conductivity to ensure efficient electron conduction and (3) stability in fuel cell operating environment. Carbon materials, such as carbon black and graphite, are commonly used as catalyst supports for PEMFCs. However, carbon-based materials are susceptible to oxidation during the fuel cell working process and start-up/shut-down cycles [1–7]:



The corrosion of the supports cause agglomeration of metal particles, resulting in a decrease of electrochemical active surface area (ECSA) of the catalysts. Furthermore, the carbon corrosion leads to a contact loss between the metal particles and the supports. As a result, the charge transfer process is inhibited. These phenomena reduce the electrocatalytic activity of fuel cell catalysts and thus, decrease the performance and durability of the fuel cells [8–14].

To overcome the drawback of carbon-based materials, there have been several efforts in searching for oxidation-resistant

non-carbon catalyst supports. Among various materials, TiO₂ has attracted researchers' attention due to its high corrosion-resistance in fuel cell working environment [15,16]. Huang et al. synthesized a Pt/mesoporous TiO₂ catalyst and tested it as a cathode electrocatalyst for an acidic PEMFC. The catalyst showed a comparable performance to that of a commercial Pt/C. After a durability test at 1.2 V for 80 h, the Pt/C catalyst lost 93% of its ECSA while the Pt/TiO₂ still kept 80% of its ECSA [15,16]. The addition of TiO₂ to Pt/C was found to improve both of its stability and catalytic activity for ORR as well as its methanol tolerance in direct methanol fuel cell (DMFC) [17,18]. Although TiO₂ showed impressive effects on the stability and activity of fuel cell catalysts, the low electrical conductivity of TiO₂ at temperatures below 200 °C inhibits its application in PEMFCs. Therefore, it is essential to improve the electronic conductivity of titania for its practical use as a promising replacement of carbon black in PEMFCs.

There are two approaches to enhance the electrical conductivity of titania. The first way is to convert TiO₂ into sub-stoichiometric titania Ti_nO_{2n-1}. The conductivity of Ti_nO_{2n-1} was reported to be highly improved, compared to TiO₂, as a result of the band gap narrowing effect of oxygen vacancies and titanium interstitials [11,19,20]. It was found that Pt supported on Ti₄O₇ showed similar activity for ORR as Pt/C, but higher stability than that of Pt/C [21–23]. However, during the fuel cell operation, sub-stoichiometric titania can be oxidized and converted to the stoichiometric one, which is nonconductive [3,4]. The second approach involves the doping of TiO₂ with a donor-type element [20]. This method creates no anion vacancy in the structure and thus, the resulting material is more stable to thermal and electrochemical

* Corresponding author. Tel.: +65 6316 8866; fax: +65 6794 7553.

E-mail address: WangXin@ntu.edu.sg (X. Wang).

oxidation [3–5]. Nb has been observed as a good donor-dopant for titania and the use of Nb-doped titania as catalyst support in acidic media has been reported [4,5,8,10,12,13,15]. In Park et al.'s study, Pt/NbTiO₂ showed a higher ORR current compared with Pt/C in 0.5 M H₂SO₄. The excellent activity of Pt/NbTiO₂ was believed to derive from the well dispersion of Pt particles on the support and an interaction between the metal catalyst and the support [13]. Chhina et al. found that rutile Nb_{0.1}Ti_{0.9}O₂ was more conductive than anatase Nb_{0.1}Ti_{0.9}O₂ while W doped-TiO₂ was much less conductive than rutile Nb_{0.1}Ti_{0.9}O₂. Pt/Nb_{0.1}Ti_{0.9}O₂ and Pt/C were examined their activity and durability as cathode catalysts in half-cell and full-cell tests. Pt/C showed a bit better ORR performance than Pt/Nb_{0.1}Ti_{0.9}O₂ before the stability test. However, the catalytic activity of Pt/C was considerably reduced after the fixed-potential test while Pt/Nb_{0.1}Ti_{0.9}O₂ nearly remained its activity after the test [4,5]. Rutile Nb-doped TiO₂ was also investigated as cathode catalyst support for PEMFC in Huang et al.'s work. At first, Nb_{0.25}Ti_{0.75}O₂ supported Pt catalyst presented similar ORR activity to that of a ETEK Pt/C. However, after an accelerated durability test by cycling between 0.6 and 1.4 V, Pt/Nb_{0.25}Ti_{0.75}O₂ showed 10-time higher ORR activity compared to Pt/C. A full-cell test indicated that Pt/C had no activity after 1000 cycles while Pt/Nb_{0.25}Ti_{0.75}O₂ only lost a small voltage (0.11 V at 0.6 A cm⁻²) after 3000 cycles [12]. In Elezovic et al.'s research, Pt/anatase Nb_{0.005}Ti_{0.995}O₂ was synthesized and investigated for its ORR activity in acidic solutions with or without the appearance of methanol. Higher ORR activity and better methanol tolerance of Pt/Nb_{0.005}Ti_{0.995}O₂ was also demonstrated [8].

Alkaline direct ethanol fuel cell (ADEFC) has been attracting more and more scientists' attention due to the high specific energy, low toxicity and easiness of mass production of ethanol from agricultural products as well as the ability of using non-platinum metals as electrocatalysts in alkaline environments [24–31]. Pd has been found to be more active for ethanol electrooxidation than Pt in alkaline condition. Moreover, it is much more abundant than Pt on earth [32–34]. Despite of its good activity for ethanol oxidation, the performance of Pd still needs to be improved. There have been some efforts to improve the performance of Pd by combining Pd with other metals, metal oxides or metal carbides [35–39]. In our previous study, the alloying Pd with Ag was found to be highly effective for the electrooxidation of ethanol in basic condition [40]. Up to date, there have been rare studies on the use and durability of Nb-doped TiO₂ as a catalyst support for ADEFCs. Besides, a systematic study of the effect of Nb ratio and synthesis temperature on the conductivity of Nb-doped TiO₂ is lacking. Therefore, in this work, we synthesized PdAg supported on Nb-doped TiO₂ with different Nb contents and investigated the effect of various Nb/Ti ratios on the conductivity, durability and catalytic activity of the catalysts for the ethanol oxidation in alkaline media. A comparison of PdAg catalysts supported on Nb-doped TiO₂, commercial TiO₂ and carbon black was carried out in the work.

2. Experimental

2.1. Preparation of Nb-doped TiO₂ with 2, 5, 10, 20 and 30% Nb

The materials were synthesized by a hydrothermal method: 4.073 g of Pluronic P123 (Aldrich) was dissolved completely in 100 ml of deionized (DI) water at 40 °C. Then 1.5 g of concentrated H₂SO₄ was added into the solution. This mixture was stirred at 40 °C. The second solution was formed from acetylacetone, niobium ethoxide and titanium isopropoxide (Aldrich); acetylacetone was added into a mixture of niobium ethoxide and titanium isopropoxide and stirred for 10 min. This solution then was added dropwise into the first solution and the mixture was stirred at 40 °C

for 30 min. A yellow powder was formed after a while. The mixture was aged at 55 °C for 12 h without stirring. Then it was transferred into a Teflon autoclave and aged at 90 °C for 24 h. The solid product was separated by filtration and washed several times by DI water. After drying at 65 °C for overnight, the solid powder was calcined at 500 °C for 4 h with a rate of 1 °C min⁻¹ in flowing air to remove the template. Then the material was annealed at high temperature for 2 h under hydrogen flow to activate Nb donor dopant in TiO₂ [4,5,12,13].

2.2. Preparation of PdAg electrocatalysts

The preparation procedure of the 10 wt% Pd–10 wt% Ag catalysts was modified from the literature [41,42]. In a typical preparation, 100 mg of a support (carbon black, commercial TiO₂, Nb_xTi_{1-x}O₂) was dispersed in 50 ml of 0.1 M NaOH in ethylene glycol (EG). Then 27 mg of Pd(NO₃)₂·xH₂O and 20 mg of AgNO₃ were added and mixed with the solution. The mixture was refluxed at 180 °C for 3 h. After reflux, the mixture was filtered or centrifuged and the solid was washed several times with DI water. Finally, it was dried at 65 °C for overnight.

2.3. Sample preparation for conductivity measurement

Pellets (diameter of 6.1 mm) were made from dry powder using a Carver hydraulic press (model 4128) with a pressure of 457 MPa. All the pellets were dried at 105 °C for overnight before conductivity measurement.

2.4. Physical and electrochemical characterization

Structure of the samples was investigated by X-ray diffraction (XRD) with a D8 Bruker AXS X-ray diffractometer (Cu K α radiation, 40 kV, 20 mA, 2 θ ranges of 20–90°, scan rate 0.025° s⁻¹).

Transmission electron microscopy (TEM, JEOL 2010) at an acceleration voltage of 200 keV was used to examine the morphology of the samples.

Electrical conductivity measurement was performed at room temperature by a two – Pt probe DC technique with an Autolab PGSTAT302 potentiostat (Eco Chemie). The electrical resistance of the samples was determined from the slopes of linear voltage vs. current curves.

N₂ adsorption/desorption isotherms were measured at –196 °C with an Autosorb 6B (Quanta Chrome). Prior to the measurement, the samples were degassed at 250 °C for overnight. The specific surface area was calculated by the Brunauer–Emmett–Teller (BET) method.

Electrochemical investigation was performed with the Autolab PGSTAT302 potentiostat using a three-electrode cell with a Pt wire and a Hg/HgO (1 M KOH) electrode as the counter and reference electrode, respectively. To prepare the working electrode for electrochemical tests, 3.3 mg of each catalyst was mixed with 1 ml of ethanol. From this mixture, 10 μ l was dropped onto a glassy carbon electrode (GCE) and the GCE was dried in air. The catalyst layer was fixed to the electrode by 5 μ l of 0.5% Nafion solution. N₂ gas was purged into the test solutions for deaeration. All current values in electrochemical results were normalized by the electrochemical active surface area (ECSA) of the catalysts determined by the PdO reduction peak of the blank cyclic voltammetry (CV) test in 1 M KOH solution with the assumption that a value of 405 mC/cm² is needed for the reduction of PdO monolayer.

2.5. Durability tests

Durability tests were carried out with a PAR VMP2 Multichannel Potentiostat (Princeton Applied Research) using two different

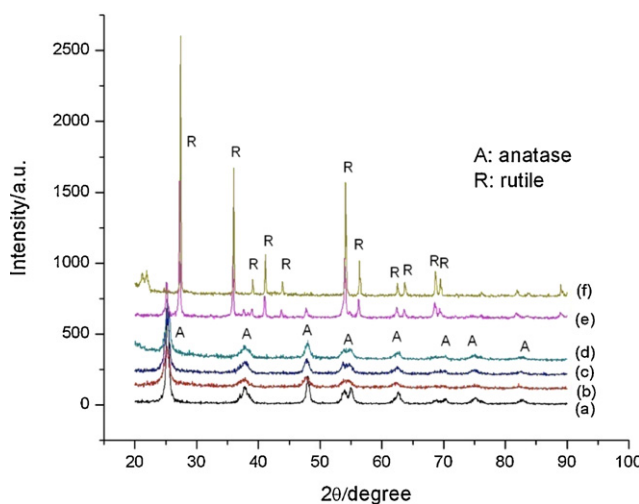


Fig. 1. XRD patterns of (a) commercial TiO_2 , (b) as-synthesized, (c) calcined $\text{Nb}_{0.10}\text{Ti}_{0.90}\text{O}_2$ and $\text{Nb}_{0.10}\text{Ti}_{0.90}\text{O}_2$ activated at (d) $400\text{ }^\circ\text{C}$, (e) $700\text{ }^\circ\text{C}$ and (f) $900\text{ }^\circ\text{C}$.

methods. (1) Potentiostatic measurement: the catalysts were kept at 0.3 and 0.7 V in N_2 purged 1 M KOH solution for 1 h. After each test, the electrochemical active surface area (ECSA) values of the catalysts were determined by CV technique. (2) Multiple CV scans: to mimic the dynamic condition, multiple CV scans in N_2 purged 1 M KOH solution were performed for each catalyst with a potential range of $-0.8\text{ V} \div 0.3\text{ V}$ and a scan rate of 50 mV s^{-1} .

3. Results and discussion

3.1. Nb-doped-TiO_2

3.1.1. $\text{Nb}_{0.10}\text{Ti}_{0.90}\text{O}_2$

Structure of commercial TiO_2 , as-synthesized, calcined $\text{Nb}_{0.10}\text{Ti}_{0.90}\text{O}_2$ and $\text{Nb}_{0.10}\text{Ti}_{0.90}\text{O}_2$ activated at different temperatures was investigated by XRD (Fig. 1). The commercial TiO_2 and the as-synthesized $\text{Nb}_{0.10}\text{Ti}_{0.90}\text{O}_2$ display typical peaks of anatase phase while the one activated at $900\text{ }^\circ\text{C}$ has a clear structure of pure rutile. After the template removal by calcination at $500\text{ }^\circ\text{C}$ and the activation at $400\text{ }^\circ\text{C}$, the material still preserve its anatase structure. However, as shown in Fig. 1e, strong peaks of rutile phase appear after the activation at $700\text{ }^\circ\text{C}$ while the peaks of anatase phase show a large decrease in intensity. It means that the structure of $\text{Nb}_{0.10}\text{Ti}_{0.90}\text{O}_2$ activated at $700\text{ }^\circ\text{C}$ is a mixture of rutile and anatase. This is consistent with previous studies [5,7,12].

Koninck et al. and Fuentes et al. found the appearance of TiNb_2O_7 in the structure of $\text{Nb}_{0.10}\text{Ti}_{0.90}\text{O}_2$ annealed at 1050 and $1000\text{ }^\circ\text{C}$ [7,43]. In our work, neither TiNb_2O_7 nor niobium oxides were observed in the XRD patterns of $\text{Nb}_{0.10}\text{Ti}_{0.90}\text{O}_2$ samples; it implies that Nb was well-incorporated into the lattice of TiO_2 . It was found that TiO_2 would form sub-stoichiometric titania $\text{T}_n\text{O}_{2n-1}$ when reduced at high temperature. However, no $\text{T}_n\text{O}_{2n-1}$ compounds were found in the XRD spectra of $\text{Nb}_{0.10}\text{Ti}_{0.90}\text{O}_2$ samples reduced at 700 and $900\text{ }^\circ\text{C}$, indicating that the addition of Nb into TiO_2 inhibits the formation of $\text{T}_n\text{O}_{2n-1}$ [5]. Crystallite sizes of the materials were calculated from the XRD patterns using Scherrer equation [5,7] based on (101) peak at $2\theta = 25.3^\circ$ for anatase and (110) peak at $2\theta = 27.5^\circ$ for rutile and presented in Table 1. The crystallite sizes of the as-synthesized, calcined $\text{Nb}_{0.10}\text{Ti}_{0.90}\text{O}_2$ and $\text{Nb}_{0.10}\text{Ti}_{0.90}\text{O}_2$ activated at $400\text{ }^\circ\text{C}$ are similar, implying that the calcination at $500\text{ }^\circ\text{C}$ and the activation at $400\text{ }^\circ\text{C}$ have little effect on the grain size. However, the crystallite size of the material sharply increases after the activation at $700\text{ }^\circ\text{C}$ (from 12.1 to 24.4 nm for anatase) and $900\text{ }^\circ\text{C}$ (from 39.3 to 59.7 nm for rutile). This phenomenon was

also observed in other works [5,7]. The increase of crystallite size is attributed to the thermally promoted grain growth [7,44].

The electrical conductivity of commercial TiO_2 and $\text{Nb}_{0.10}\text{Ti}_{0.90}\text{O}_2$ materials was measured at room temperature and presented in Table 1. The measured conductivity of the commercial TiO_2 is $4.9 \times 10^{-8}\text{ S cm}^{-1}$, which is in high agreement with values (10^{-13} , 10^{-6} S cm^{-1}) in the literature [13,20]. The calcined $\text{Nb}_{0.10}\text{Ti}_{0.90}\text{O}_2$ has a slightly higher conductivity of $2.3 \times 10^{-7}\text{ S cm}^{-1}$. The reduction of calcined $\text{Nb}_{0.10}\text{Ti}_{0.90}\text{O}_2$ at 400 , 700 and $900\text{ }^\circ\text{C}$ greatly improved the electronic conductivity of the material, as indicated by their measured conductivity (1.9×10^{-6} , 7.9×10^{-5} and 0.001 S cm^{-1} , respectively).

To examine the porosity of the materials, N_2 adsorption/desorption isotherms were measured at $-196\text{ }^\circ\text{C}$ and the results are shown in Fig. 2 and Table 1. The commercial TiO_2 shows a N_2 adsorption/desorption isotherm with a narrow hysteresis loop due to its poor porosity. Fig. 2b shows a typical type-IV isotherm with a large H2 hysteresis loop caused by mesopores with interconnecting channels in the structure of the as-synthesized $\text{Nb}_{0.10}\text{Ti}_{0.90}\text{O}_2$ [16,45]. As shown in Fig. 2c and d, the material maintained its mesoporosity after the calcination at $500\text{ }^\circ\text{C}$ and activation at $400\text{ }^\circ\text{C}$ with unchanged isotherm shape although its BET surface area slightly decreased from 211 to 182 and $142\text{ m}^2\text{ g}^{-1}$, respectively. After the activation at $700\text{ }^\circ\text{C}$, the isotherm of the solid shows a narrower H1 hysteresis loop with nearly vertical and parallel adsorption and desorption branches, which is attributed to mesopores without interconnecting channels [45]. The reduction at $700\text{ }^\circ\text{C}$ caused a collapse of the interconnecting channels, resulting in a sharp decrease of BET area from 182 to $30\text{ m}^2\text{ g}^{-1}$. The solid reduced at $900\text{ }^\circ\text{C}$ displays a nitrogen adsorption/desorption isotherm with no typical characteristics of mesopores, indicating that the ordered mesoporous structure was destroyed. As a result, the BET area was reduced to $20\text{ m}^2\text{ g}^{-1}$. Considering the values of electrical conductivity and porosity of the materials, the Nb-doped TiO_2 activated at $700\text{ }^\circ\text{C}$ was chosen for further study due to the potential benefit of its high conductivity and mesoporous structure for the application as electrocatalyst support in ADFEC.

3.1.2. $\text{Nb}_x\text{Ti}_{1-x}\text{O}_2$

As shown above, the addition of Nb into TiO_2 structure significantly enhanced the conductivity of TiO_2 . Therefore, we synthesized various Nb-doped TiO_2 with different Nb contents (2, 5, 10, 20 and 30%) and investigated the effect of Nb-doping level to their properties. All the $\text{Nb}_x\text{Ti}_{1-x}\text{O}_2$ materials were calcined at $500\text{ }^\circ\text{C}$ in air flow and then activated at $700\text{ }^\circ\text{C}$ in H_2 flow. XRD patterns of the Nb-doped TiO_2 solids are displayed in Fig. 3 with reference spectra of anatase and rutile TiO_2 (JCPDS 21-1272 and 65-0191, respectively). A mixture of rutile and anatase phases is observed for all the $\text{Nb}_x\text{Ti}_{1-x}\text{O}_2$ materials. It can be found that the diffraction peaks of $\text{Nb}_x\text{Ti}_{1-x}\text{O}_2$ are shifted to lower angles when Nb-doping level increases. This phenomenon indicates an increase in unit-cell parameters of the material due to the replacement of Ti^{4+} ($r_{\text{Ti}^{4+}} = 60.5\text{ pm}$) by larger ion Nb^{5+} ($r_{\text{Nb}^{5+}} = 64\text{ pm}$) [5,46–49]. Table 2 shows the lattice constants of Nb-doped TiO_2 obtained by fitting XRD patterns of $\text{Nb}_x\text{Ti}_{1-x}\text{O}_2$ with anatase and rutile structures using PowderCell 2.4 software developed by Kraus and Nolze [47,50]. The values of lattice constants again confirm the fact that unit cells of titania expanded their volume after the addition of Nb. The highest expansion is observed for $\text{Nb}_x\text{Ti}_{1-x}\text{O}_2$ with 30% of Nb. Crystallite sizes of the materials were calculated using Scherrer equation and displayed in Table 2. The results show a decreasing trend in the crystallite size of both anatase and rutile phases when increasing Nb content from 2 to 30%. It is believed that the presence of Nb in titania structure inhibits the growth of crystallites [7,51].

The electronic conductivity of $\text{Nb}_x\text{Ti}_{1-x}\text{O}_2$ was measured and shown in Table 2 and Fig. 4. The addition of Nb to TiO_2 lattice

Table 1Properties of commercial TiO_2 and $\text{Nb}_{0.10}\text{Ti}_{0.90}\text{O}_2$ materials.

Material	Crystallite size (nm)		BET surface area ($\text{m}^2 \text{g}^{-1}$)	Conductivity (S cm^{-1})
	Anatase	Rutile		
Commercial TiO_2	17.1		266	4.9×10^{-8}
$\text{Nb}_{0.10}\text{Ti}_{0.90}\text{O}_2$				
As-synthesized	11.9		211	n/a
Calcined at 500 °C	13.0		182	2.3×10^{-7}
Activated at 400 °C	12.1		142	1.9×10^{-6}
Activated at 700 °C	24.4	36.3	30	7.9×10^{-5}
Activated at 900 °C		59.7	20	0.001

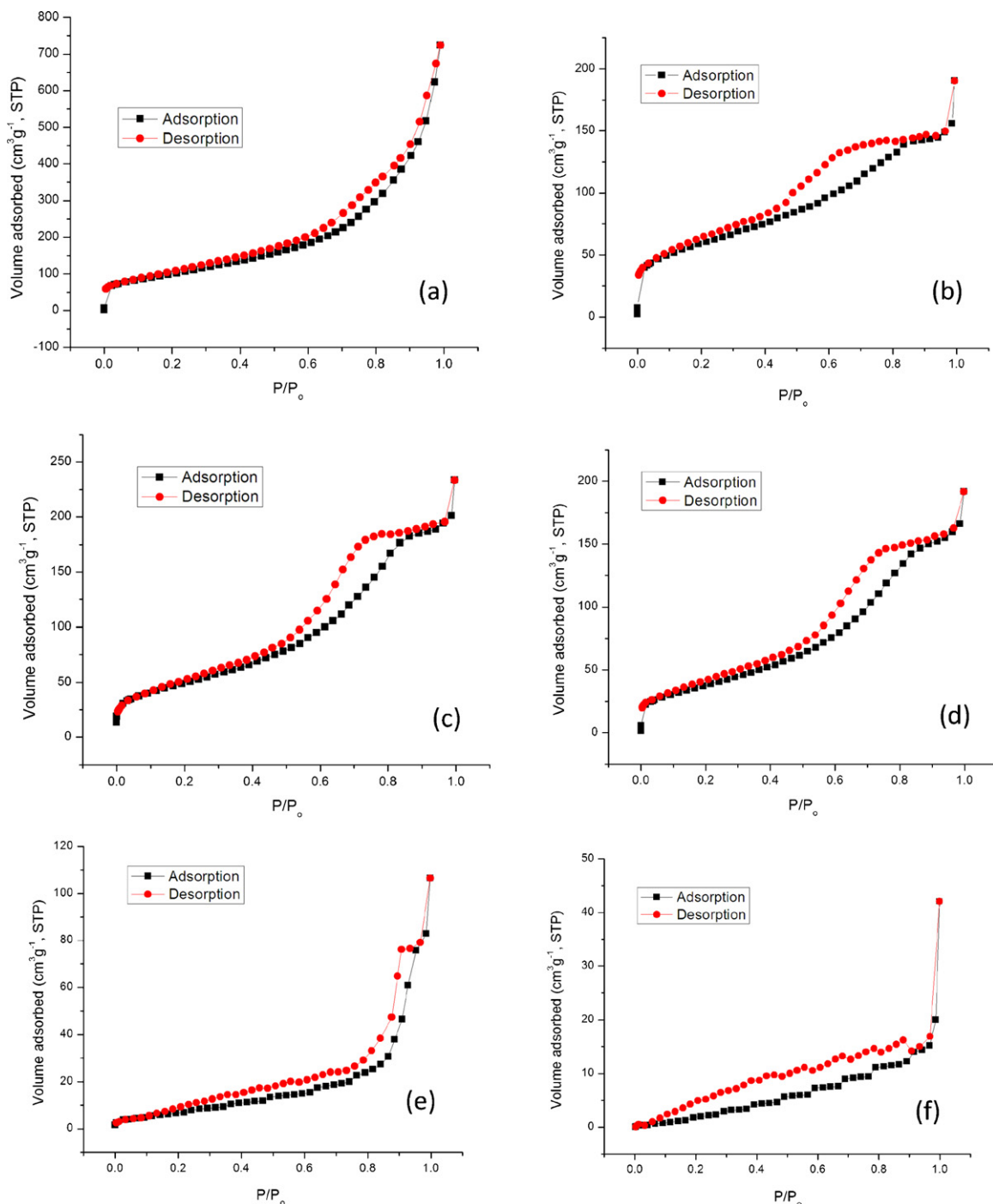
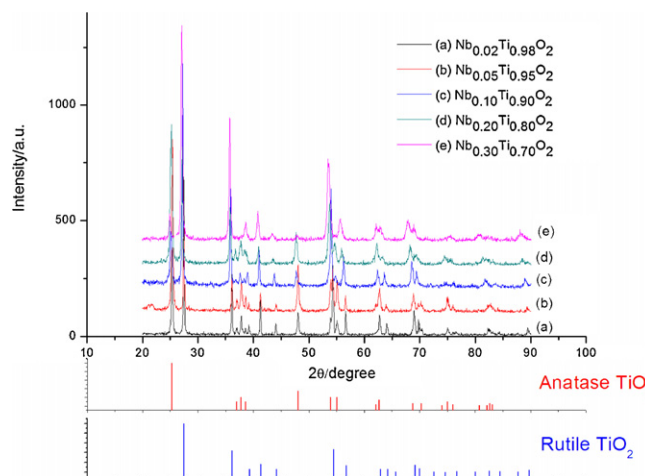
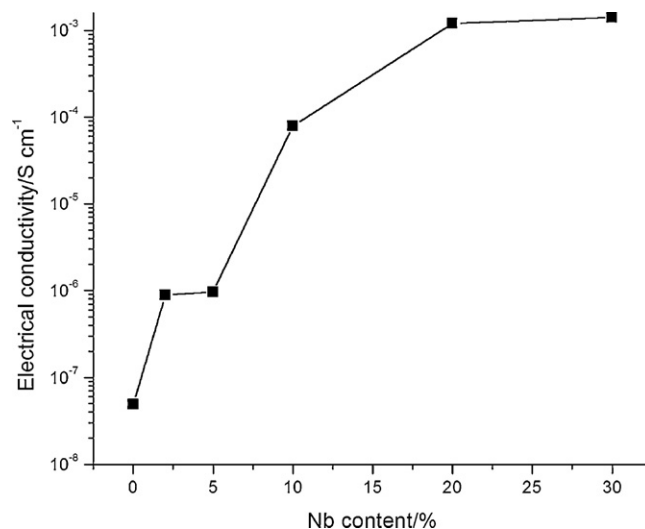
**Fig. 2.** Nitrogen adsorption/desorption isotherms of (a) commercial TiO_2 , (b) as-synthesized, (c) calcined $\text{Nb}_{0.10}\text{Ti}_{0.90}\text{O}_2$ and $\text{Nb}_{0.10}\text{Ti}_{0.90}\text{O}_2$ activated at (d) 400 °C, (e) 700 °C and (f) 900 °C.

Table 2Properties of $\text{Nb}_x\text{Ti}_{1-x}\text{O}_2$ materials compared with commercial TiO_2 .

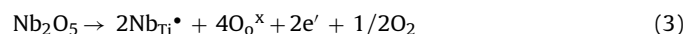
Material	Lattice constant (nm)		Crystallite size (nm)		BET surface area ($\text{m}^2 \text{g}^{-1}$)	Conductivity (S cm^{-1})
	Anatase	Rutile	Anatase	Rutile		
Commercial TiO_2	$a=b=0.37853$ $c=0.95070$		17.1		266	4.9×10^{-8}
$\text{Nb}_{0.02}\text{Ti}_{0.98}\text{O}_2$	$a=b=0.37864$ $c=0.95190$	$a=b=0.45979$ $c=0.29611$	33.0	45.7	22	8.9×10^{-7}
$\text{Nb}_{0.05}\text{Ti}_{0.95}\text{O}_2$	$a=b=0.37909$ $c=0.95246$	$a=b=0.46033$ $c=0.29637$	28.0	39.9	31	9.6×10^{-7}
$\text{Nb}_{0.10}\text{Ti}_{0.90}\text{O}_2$	$a=b=0.38170$ $c=0.95263$	$a=b=0.46380$ $c=0.29804$	24.4	36.3	30	7.9×10^{-5}
$\text{Nb}_{0.20}\text{Ti}_{0.80}\text{O}_2$	$a=b=0.38261$ $c=0.95501$	$a=b=0.46504$ $c=0.29847$	23.0	30.5	36	0.0012
$\text{Nb}_{0.30}\text{Ti}_{0.70}\text{O}_2$	$a=b=0.38326$ $c=0.95774$	$a=b=0.46607$ $c=0.29937$	21.7	25.6	46	0.0014

**Fig. 3.** XRD patterns of $\text{Nb}_x\text{Ti}_{1-x}\text{O}_2$ activated at 700°C with $x = 0.02$ (a), 0.05 (b), 0.10 (c), 0.20 (d) and 0.30 (e).

structure dramatically improved the conductivity of the material from $4.9 \times 10^{-8} \text{ S cm}^{-1}$ of anatase TiO_2 to 8.9×10^{-7} , 9.6×10^{-7} , 7.9×10^{-5} , 0.0012 and 0.0014 S cm^{-1} of Nb-doped TiO_2 with Nb contents of 2, 5, 10, 20 and 30%, respectively. TiO_2 has large band gaps (3.2 eV of anatase and 3.0 eV of rutile), which result in its low electrical conductivity [12,13,51]. Nb atom has five outer-shell electrons. When it substitutes Ti sites in TiO_2 lattice, only four electrons

**Fig. 4.** Electrical conductivity of $\text{Nb}_x\text{Ti}_{1-x}\text{O}_2$ with different Nb contents.

are used for bonding. The extra electron is in donor state which is 0.02–0.03 eV below the conduction band minimum and therefore, is easy to be donated into the conduction band to increase the charge carrier concentration [12,48,52]. As a result, Nb doping enhances the electronic conductivity of the material:



However, it can be seen that the conductivity of Nb-doped TiO_2 with 30% of Nb (0.0014 S cm^{-1}) is only a bit higher than that of the one with 20% of Nb (0.0012 S cm^{-1}). This phenomenon is consistent with the literature [46]. This fact can be explained by several possible ways. Firstly, when Nb is doped into TiO_2 lattice, the Fermi energy will move towards the conduction band. Consequently, the formation energy of Ti vacancy will decrease. At some points, this formation energy is so low that Ti vacancies will form spontaneously (Eq. (4)) and weaken the donor effect (Eq. (3)) [46,53,54].



Secondly, the substitution of Nb for Ti can also create oxygen interstitials – another type of electron killer, which reduce the electronic conductivity of Nb-doped TiO_2 . Thirdly, the incorporation of Nb into the titania structure also causes a lattice deformation, which can lead to a decrease in electron mobility [46,52–54].

The porosity of the $\text{Nb}_x\text{Ti}_{1-x}\text{O}_2$ materials was examined by N_2 adsorption/desorption at -196°C and the results are displayed in Fig. 5 and Table 2. Adsorption/desorption isotherms of all the solids have the same shape as that of $\text{Nb}_{0.10}\text{Ti}_{0.90}\text{O}_2$ indicating that all of them possess mesoporous structures with no interconnecting channels. It can be observed that BET area of the $\text{Nb}_x\text{Ti}_{1-x}\text{O}_2$ solids increases with the raise of Nb-doping level. The lowest area of $22 \text{ m}^2 \text{ g}^{-1}$ was found for $\text{Nb}_{0.02}\text{Ti}_{0.98}\text{O}_2$ while the maximum value of $36 \text{ m}^2 \text{ g}^{-1}$ was seen with $\text{Nb}_{0.30}\text{Ti}_{0.70}\text{O}_2$. As stated previously, the Nb doping prevents the grain growth, and thus, increases the BET specific surface area of $\text{Nb}_x\text{Ti}_{1-x}\text{O}_2$ [7].

3.2. PdAg/Nb-doped TiO_2

Fig. 6 shows XRD profiles of PdAg alloy supported on carbon black, commercial TiO_2 and various $\text{Nb}_x\text{Ti}_{1-x}\text{O}_2$. PdAg/C displays typical (111), (200), (220) and (311) peaks of face-centered cubic (FCC) structure of PdAg alloy at 38.8° , 44.6° , 65.5° and 78.8° . In XRD patterns of PdAg/commercial TiO_2 and PdAg/ $\text{Nb}_x\text{Ti}_{1-x}\text{O}_2$, the peaks of PdAg alloy are overlapped by strong diffraction peaks of the supports.

The electrocatalytic activity for ethanol oxidation of the catalysts was examined in an aqueous solution of 1 M $\text{C}_2\text{H}_5\text{OH}$ and 1 M KOH by cyclic voltammetry (CV) technique and the results are shown in Fig. 7. PdAg supported on commercial TiO_2 and $\text{Nb}_x\text{Ti}_{1-x}\text{O}_2$ show a 75 mV more negative onset potential for ethanol

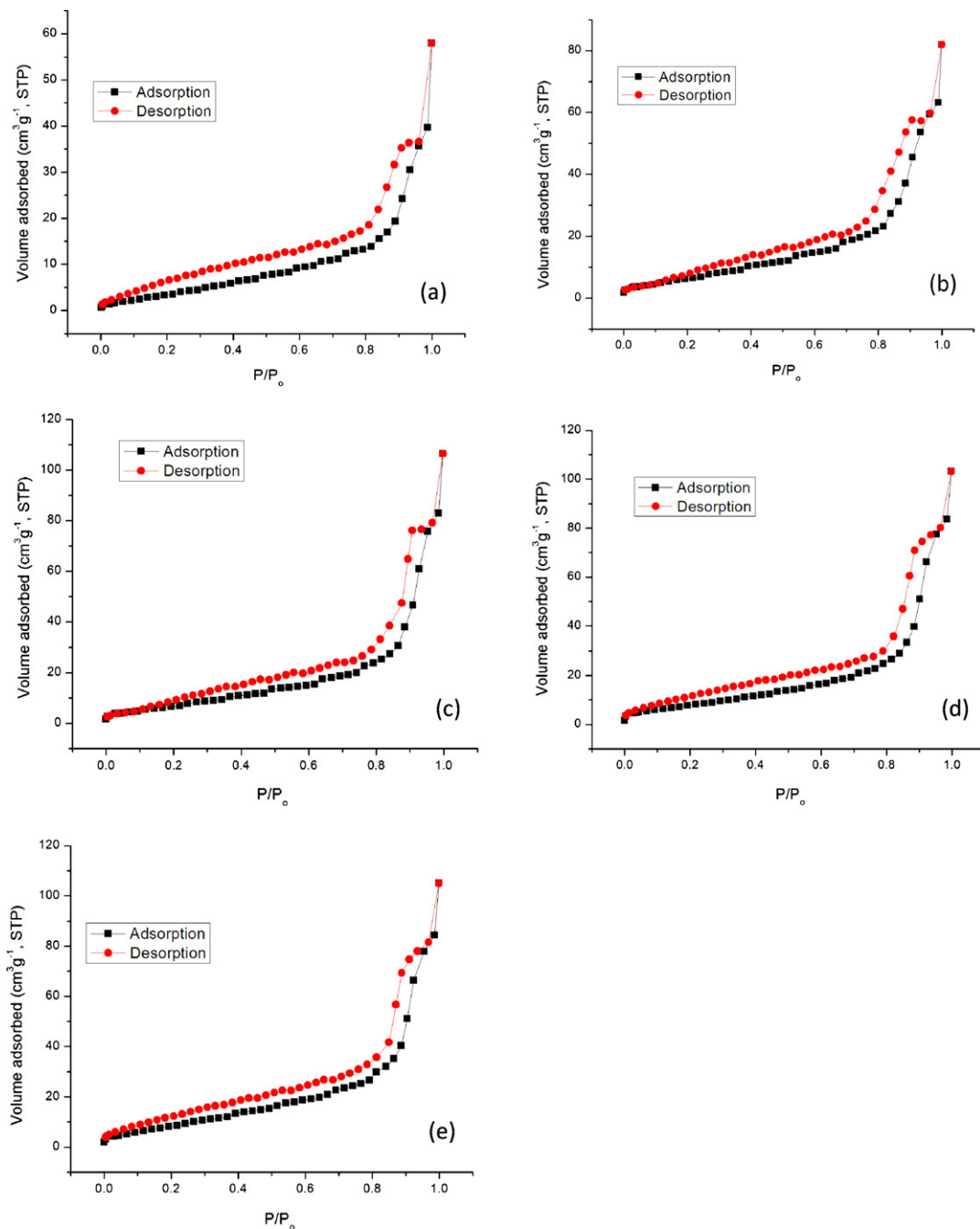


Fig. 5. Nitrogen adsorption/desorption isotherms of $\text{Nb}_x\text{Ti}_{1-x}\text{O}_2$ activated at 700°C with $x = 0.02$ (a), 0.05 (b), 0.10 (c), 0.20 (d) and 0.30 (e).

oxidation compared to that of PdAg/C. This proves the enhancement effect of TiO_2 and $\text{Nb}_x\text{Ti}_{1-x}\text{O}_2$ to the catalytic property of the catalyst. On the other hand, PdAg/ $\text{Nb}_x\text{Ti}_{1-x}\text{O}_2$ catalysts have higher peak current density than that of PdAg/ TiO_2 with the best behavior observed for PdAg/ $\text{Nb}_{0.20}\text{Ti}_{0.80}\text{O}_2$ and PdAg/ $\text{Nb}_{0.30}\text{Ti}_{0.70}\text{O}_2$. As proposed by Hammer and Nørskov, the electronic structure of small metal particles supported on substrates is altered by the interaction between the substrates and the nanoparticles due to lattice constant mismatch, which results in a change in their adsorption and catalytic activity [8,55,56]. From the XRD data of (200) peak, the lattice constant value of the PdAg alloy supported on carbon black was found at 0.403 nm. This value is smaller than those (c

for anatase and a,b for rutile) of $\text{Nb}_x\text{Ti}_{1-x}\text{O}_2$ presented in Table 2. Therefore, an expansion of the unit-cell of the alloy is created when the alloy nanoparticle is deposited on the Nb-doped TiO_2 support. As a result, d-band center of the alloy moves up and the adsorption of OH^- on the catalyst surface is improved [57,58]. According to Liang et al. [59], the adsorbed OH^- plays an important role in the removal of CH_3CO to release active sites for further ethanol electrooxidation process. Hence, the improvement of OH^- adsorption leads to a faster ethanol oxidation. Experimental evidence for the improved OH^- adsorption is presented in Fig. 10. A broad peak at ca. -0.300 V in forward scans is assigned to the adsorption of OH^- on the catalysts while the peak at ca. -0.230 V in reverse scans belongs

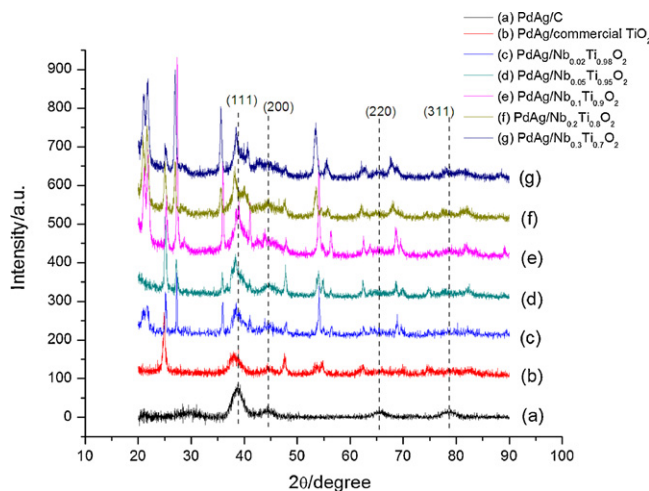


Fig. 6. XRD profiles of PdAg/C (a), PdAg/commercial TiO₂ (b), PdAg/Nb_xTi_{1-x}O₂ with $x = 0.02$ (c), 0.05 (d), 0.10 (e), 0.20 (f) and 0.30 (g).

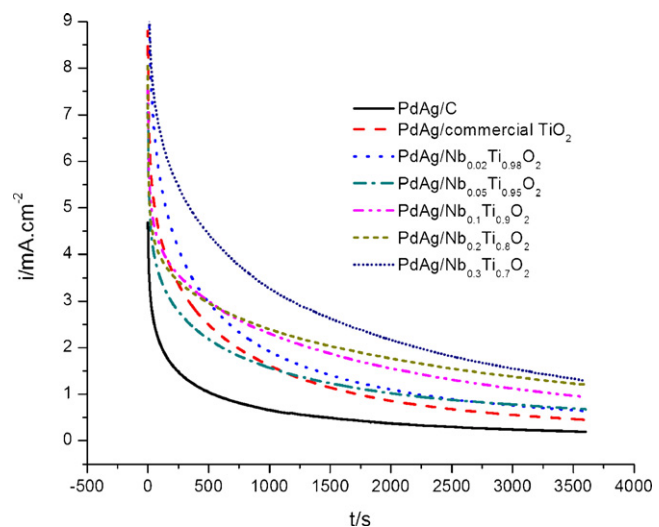


Fig. 8. CA results of PdAg/C, PdAg/commercial TiO₂, PdAg/Nb_xTi_{1-x}O₂ with $x = 0.02$, 0.05, 0.10, 0.20 and 0.30 at -0.25 V (vs. Hg/HgO) in 1 M C₂H₅OH + 1 M KOH solution.

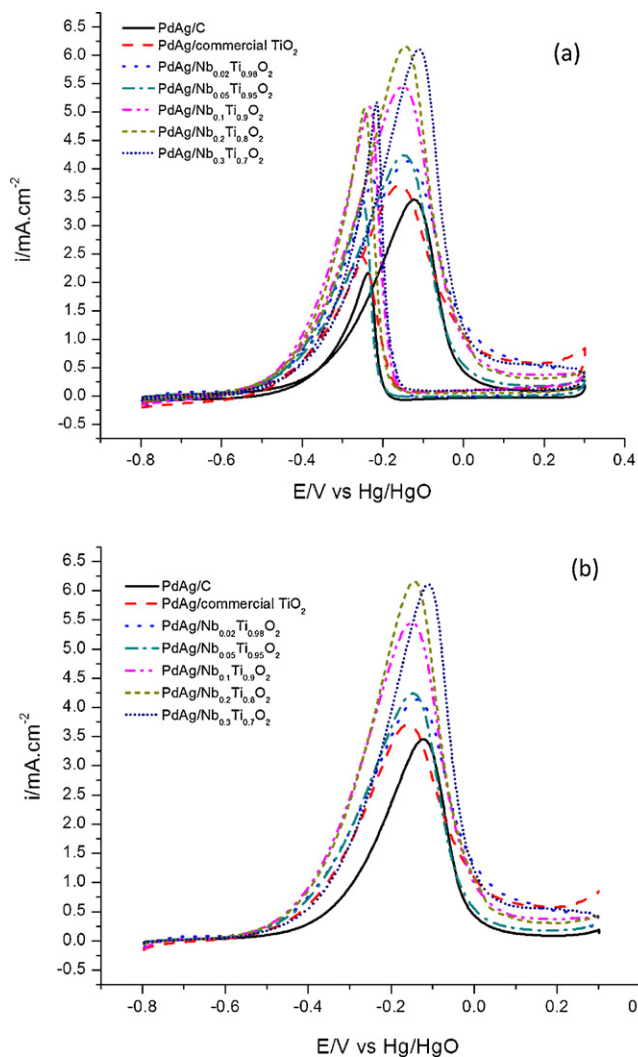


Fig. 7. (a) CVs and (b) forward scans of CV of PdAg/C, PdAg/commercial TiO₂, PdAg/Nb_xTi_{1-x}O₂ with $x = 0.02$, 0.05, 0.10, 0.20 and 0.30 in 1 M KOH + 1 M C₂H₅OH solution, scan rate of 50 mV s⁻¹.

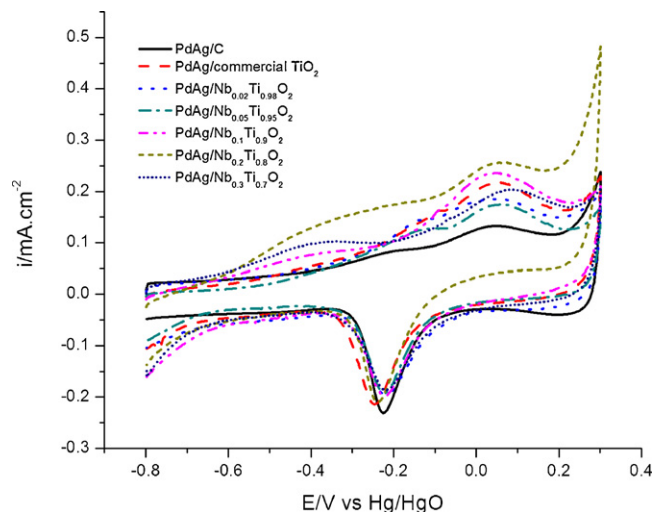


Fig. 9. CO stripping curves of PdAg/C, PdAg/commercial TiO₂, PdAg/Nb_xTi_{1-x}O₂ with $x = 0.02$, 0.05, 0.10, 0.20 and 0.30 in 1 M KOH solution, scan rate of 50 mV s⁻¹.

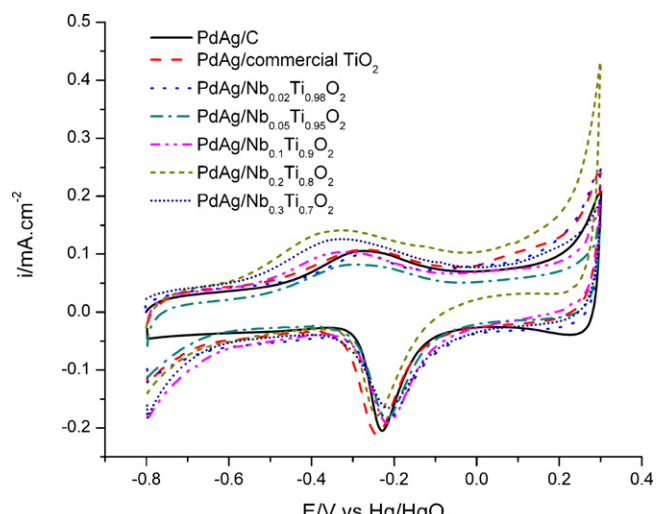


Fig. 10. Blank CVs of PdAg/C, PdAg/commercial TiO₂, PdAg/Nb_xTi_{1-x}O₂ with $x = 0.02$, 0.05, 0.10, 0.20 and 0.30 in 1 M KOH solution, scan rate of 50 mV s⁻¹.

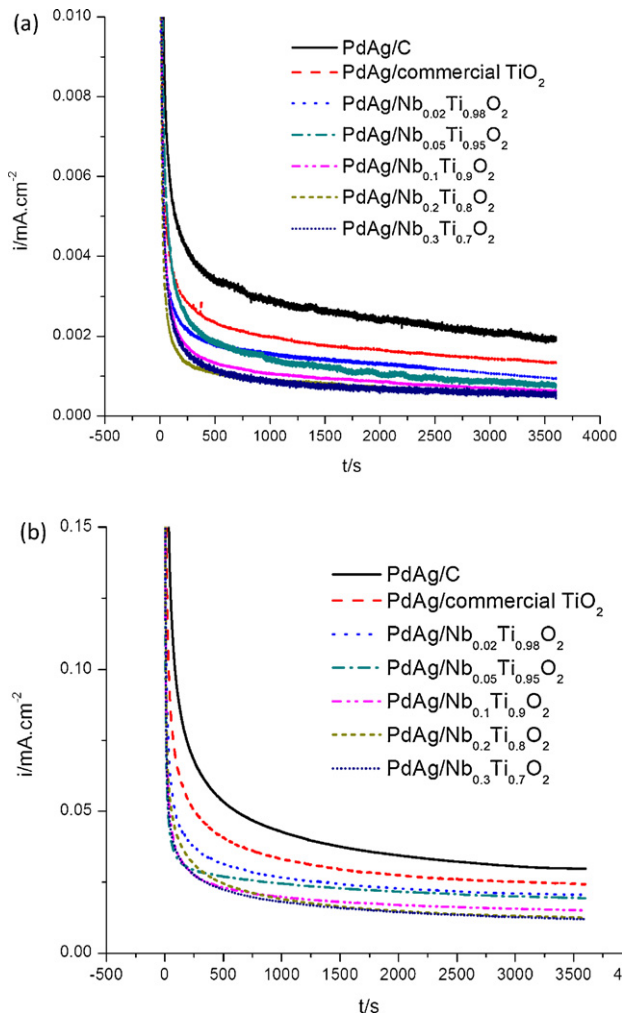


Fig. 11. Corrosion curves of PdAg/C, PdAg/commercial TiO₂, PdAg/Nb_xTi_{1-x}O₂ with $x=0.02, 0.05, 0.10, 0.20$ and 0.30 in 1 M KOH solution at (a) 0.3 V and (b) 0.7 V , 1 h .

to the reduction of palladium oxide. The hydroxyl adsorption peak potentials are $-0.270, -0.273, -0.279, -0.298, -0.310, -0.326$ and -0.332 V for PdAg supported on carbon black, commercial TiO₂, Nb-doped TiO₂ with 2, 5, 10, 20 and 30% of Nb, respectively. It can be observed that with the increase of Nb content, the peak potential of OH⁻ adsorption shifts negatively, indicating an easier adsorption of OH⁻.

The activity and stability of PdAg/C, PdAg/commercial TiO₂ and PdAg/Nb_xTi_{1-x}O₂ for ethanol oxidation were also examined by CA tests. Fig. 8 shows CA curves of the catalysts in $1 \text{ M KOH} + 1 \text{ M C}_2\text{H}_5\text{OH}$ solution for 3600 s at -0.25 V . The current densities are gradually decayed with time due to the accumulation of poisoning intermediates of the ethanol oxidation process and the corrosion of the supports. After 3600 s , the current densities of PdAg/Nb_xTi_{1-x}O₂ remain higher than those of PdAg/TiO₂ and PdAg/C with the highest values observed for PdAg/Nb_{0.20}Ti_{0.80}O₂ and PdAg/Nb_{0.30}Ti_{0.70}O₂, indicating that the addition of Nb to TiO₂ facilitates the removal of the adsorbed ethoxy intermediates and helps the catalysts be more resistant to poisoning as well as Nb_xTi_{1-x}O₂ has better corrosion-resistance than carbon black in the tested solution. Further stability tests will be done in the following sections to verify the higher durability of the Nb_xTi_{1-x}O₂ materials.

CO-like species are known as the main poisoning intermediates during alcohol electrooxidation. Therefore, for better understand the poisoning tolerance of the PdAg supported on Nb-doped TiO₂ catalysts in alkaline media, CO stripping test was performed in

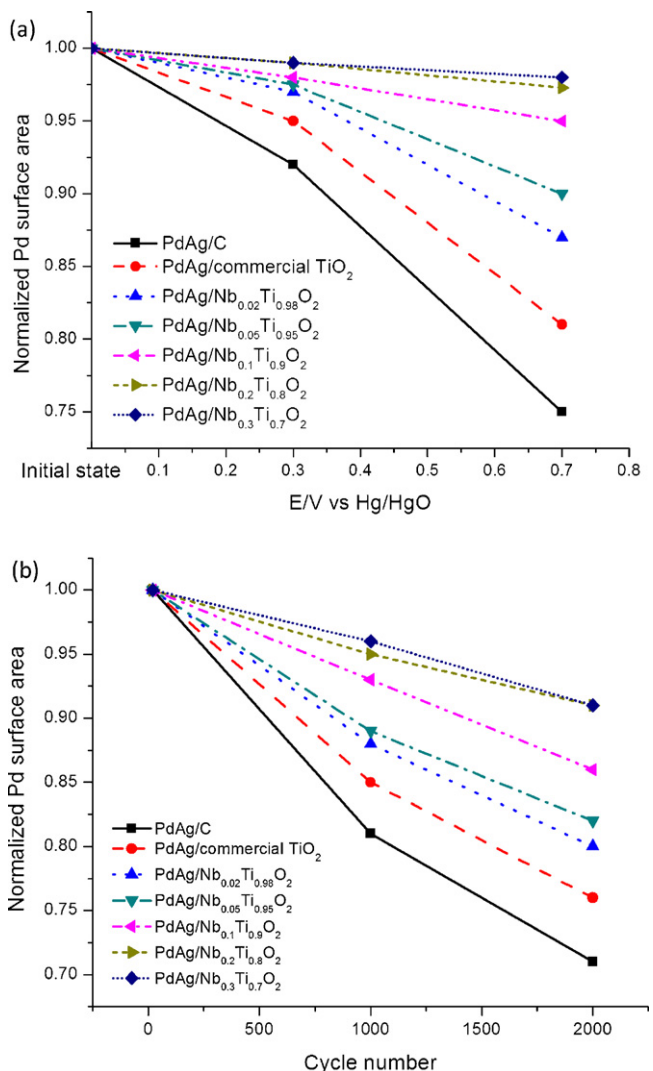


Fig. 12. Normalized Pd ECSAs of PdAg/C, PdAg/commercial TiO₂, PdAg/Nb_xTi_{1-x}O₂ with $x=0.02, 0.05, 0.10, 0.20$ and 0.30 after (a) fixed-potential and (b) multi-scan tests.

1 M KOH solution. Fig. 9 presents CO stripping curves of the catalysts. All the CO stripping profiles of the PdAg catalysts display two broad peaks due to two different types of Pd sites, which is consistent with what was found in our previous work [40]. It can be seen that onset potential values of the CO oxidation on PdAg/Nb_xTi_{1-x}O₂ are more negative than those of PdAg/C and PdAg/TiO₂ with the most negative ones observed for PdAg/Nb_{0.20}Ti_{0.80}O₂ and PdAg/Nb_{0.30}Ti_{0.70}O₂. These results again confirm the good poisoning-tolerance of the PdAg supported on Nb_xTi_{1-x}O₂.

Finally, the stability of the catalyst was examined by both potentiostatic measurement and multiple CV scans. Fig. 11 shows corrosion current densities of the PdAg catalysts at 0.3 (Fig. 11a) and 0.7 V (Fig. 11b). In both cases, the lowest corrosion current densities are found for PdAg supported on Nb-doped TiO₂ with Nb content of 20 and 30% while the highest ones are observed for PdAg supported on carbon black. The corrosion current density values of the catalysts at 0.7 V are approximately 20-time higher than those at 0.3 V , indicating the considerable effect of the potential to the corrosion of catalysts. Pd ECSAs of the catalysts after the tests normalized by the initial ones are plotted against the tested potentials in Fig. 12a. It is found that PdAg/C and PdAg/commercial TiO₂ lost 25 and 19% of their ECSA, respectively, while PdAg/Nb_xTi_{1-x}O₂ only

lost 13, 10, 5, 2.7 and 2% of their ECSA, corresponding to Nb percentages of 2, 5, 10, 20 and 30%, respectively, after the durability test at 0.7 V. The results confirm the weak stability of carbon black and strong corrosion-resistance of Nb-doped TiO₂ materials in the alkaline condition.

In the second way for investigating the durability of the catalysts, multiple CV scans were performed and Pd ECSA of each catalyst was recorded after the test to evaluate their oxidation resistance under dynamic condition. As presented in Fig. 12b, PdAg/C lost 19% and 29% of its Pd ECSA after 1000 and 2000 scans, respectively. Meanwhile, losses of 15 and 24% of Pd ECSA were found for PdAg/commercial TiO₂. The PdAg supported on Nb_xTi_{1-x}O₂ shows less corrosion with a decreasing trend in Pd ECSA loss when increasing Nb content in Nb-doped TiO₂. PdAg/Nb_{0.02}Ti_{0.98}O₂ lost 12 and 20% of Pd ECSA after 1000 and 2000 scans, respectively, while ECSAs of PdAg/Nb_{0.20}Ti_{0.80}O₂ and PdAg/Nb_{0.30}Ti_{0.70}O₂ decreased 5 and 4% after 1000 scans, respectively, and 9% after 2000 scans. As stated above, the corrosion of the supports causes the detachment of the alloy particles from the supports as well as their agglomeration and the decrease of the charge transfer between the catalyst particles and the conductive support, which results in the ECSA and activity loss. The smaller Pd ECSA loss of PdAg/Nb_xTi_{1-x}O₂ compared with those of PdAg/C and PdAg/TiO₂ during the corrosion tests proves that Nb-doped TiO₂ supports are electrochemically more stable than carbon black and commercial TiO₂.

4. Conclusions

In this research, mesoporous Nb-doped TiO₂ materials were successfully synthesized and tested as catalyst supports for PdAg nanoparticles. 700 °C was chosen as the suitable activation temperature for Nb-doped titania. The structure of Nb-doped TiO₂ activated at 700 °C consists of a mixture of rutile and anatase phases. The addition of Nb into TiO₂ structure significantly improves the electronic conductivity of TiO₂. It was found that an increase of Nb content in Nb-doped TiO₂ results in an increase in electrical conductivity of the material. PdAg supported on various Nb_xTi_{1-x}O₂ with x = 0.02, 0.05, 0.10, 0.20 and 0.30 were synthesized and their activity and durability for ethanol electrooxidation in alkaline solutions were compared with those of PdAg/C and PdAg/commercial TiO₂. The PdAg/Nb_xTi_{1-x}O₂ displayed better performance for ethanol oxidation than PdAg/C and PdAg/TiO₂. PdAg supported on Nb_{0.20}Ti_{0.80}O₂ and Nb_{0.30}Ti_{0.70}O₂ showed the highest catalytic activity towards ethanol oxidation as well as excellent durability in basic solutions. The results indicated that Nb_xTi_{1-x}O₂ materials can be used as an effective replacement for carbon black in the role of catalyst support for ADEFC. Further investigation with single fuel cells will be carried out for the Nb_xTi_{1-x}O₂-supported PdAg catalysts to determine their behavior in actual ADEFCs.

Acknowledgements

We would like to thank Singapore Ministry of Education (Academic Research Fund ARC 2/10 (MOE2009-T2-2-024)) and Singapore National Research Foundation (Competitive Research Program-2009 NRF-CRP 001-032) for their financial supports. A scholarship for Mr. Son Truong Nguyen from AUN/SEEDNet-JICA is gratefully acknowledged.

References

- [1] E. Antolini, Applied Catalysis B: Environmental 100 (2010) 413–426.
- [2] E. Antolini, E.R. Gonzalez, Solid State Ionics 180 (2009) 746–763.
- [3] G. Chen, S.R. Bare, T.E. Mallouk, Journal of the Electrochemical Society 149 (2002) A1092–A1099.
- [4] H. Chhina, S. Campbell, O. Kesler, Journal of the Electrochemical Society 156 (2009) B1232–B1237.
- [5] X. Wang, W.Z. Li, Z. Chen, M. Waje, Y.S. Yan, Journal of Power Sources 158 (2006) 154–159.
- [6] T.B. Do, M. Cai, M.S. Ruthkosky, T.E. Moylan, Electrochimica Acta 55 (2010) 8013–8017.
- [7] M.D. Koninck, P. Manseau, B. Marsan, Journal of Electroanalytical Chemistry 611 (2007) 67–79.
- [8] N.R. Elezovic, B.M. Babic, L. Gajic-Krstajic, V. Radmilovic, N.V. Krstajic, L.J. Vrancar, Journal of Power Sources 195 (2010) 3961–3968.
- [9] R.E. Fuentes, B.L. Garcia, J.W. Weidner, ECS Transactions 12 (2008) 239–248.
- [10] B.L. Garcia, R. Fuentes, J.W. Weidner, Electrochemical and Solid-State Letters 10 (2007) B108–B110.
- [11] S.L. Gojkovic, B.M. Babic, V.R. Radmilovic, N.V. Krstajic, Journal of Electroanalytical Chemistry 639 (2010) 161–166.
- [12] S.Y. Huang, P. Ganeshan, B.N. Popov, Applied Catalysis B: Environmental 96 (2010) 224–231.
- [13] K.W. Park, K.S. Seol, Electrochemistry Communications 9 (2007) 2256–2260.
- [14] J. Wang, G. Yin, Y. Shao, S. Zhang, Z. Wang, Y. Gao, Journal of Power Sources 171 (2007) 331–339.
- [15] S.Y. Huang, P. Ganeshan, S. Park, B.N. Popov, Journal of the American Chemical Society 131 (2009) 13898–13899.
- [16] S.Y. Huang, P. Ganeshan, P. Zhang, B.N. Popov, ECS Transactions 25 (2009) 1893–1902.
- [17] S.V. Selvaganesh, G. Selvarani, P. Sridhar, S. Pitchumani, A.K. Shukla, Journal of the Electrochemical Society 157 (2010) B1000–B1007.
- [18] G. Selvarani, S. Maheswari, P. Sridhar, S. Pitchumani, A.K. Shukla, Journal of the Electrochemical Society 156 (2009) B1354–B1360.
- [19] M. Radecka, A. Trenczek-Zajac, K. Zakrzewska, M. Rekas, Journal of Power Sources 173 (2007) 816–821.
- [20] Y. Shao, J. Liu, Y. Wang, Y. Lin, Journal of Materials Chemistry 19 (2009) 46–59.
- [21] T. Ioroi, H. Senoh, Z. Siroma, S. Yamazaki, N. Fujiwara, K. Yasuda, ECS Transactions 11 (2007) 1041–1048.
- [22] T. Ioroi, H. Senoh, S.I. Yamazaki, Z. Siroma, N. Fujiwara, K. Yasuda, Journal of the Electrochemical Society 155 (2008) B321–B326.
- [23] T. Ioroi, Z. Siroma, N. Fujiwara, S.I. Yamazaki, K. Yasuda, Electrochemistry Communications 7 (2005) 183–188.
- [24] Y. Wang, T.S. Nguyen, C. Wang, X. Wang, Dalton Transactions (2009) 7606–7609.
- [25] Y. Wang, T.S. Nguyen, X.W. Liu, X. Wang, Journal of Power Sources 195 (2010) 2619–2622.
- [26] N. Fujiwara, Z. Siroma, S.I. Yamazaki, T. Ioroi, H. Senoh, K. Yasuda, Journal of Power Sources 185 (2008) 621–626.
- [27] E. Antolini, E.R. Gonzalez, Journal of Power Sources 195 (2010) 3431–3450.
- [28] J. Lobato, P. Cañizares, M.A. Rodrigo, J.J. Linares, Applied Catalysis B: Environmental 91 (2009) 269–274.
- [29] Y. Wang, X. Wang, C.M. Li, Applied Catalysis B: Environmental 99 (2010) 229–234.
- [30] J. Lobato, P. Cañizares, D. Ubeda, F.J. Pinar, M.A. Rodrigo, Applied Catalysis B: Environmental 106 (2011) 174–180.
- [31] S. Song, P. Tsiaikaris, Applied Catalysis B: Environmental 63 (2006) 187–193.
- [32] C. Xu, P.K. Shen, Y. Liu, Journal of Power Sources 164 (2007) 527–531.
- [33] J. Ye, J. Liu, C. Xu, S.P. Jiang, Y. Tong, Electrochemistry Communications 9 (2007) 2760–2763.
- [34] H. Liu, W. Li, A. Manthiram, Applied Catalysis B: Environmental 90 (2009) 184–194.
- [35] P.K. Shen, C. Xu, Electrochemistry Communications 8 (2006) 184–188.
- [36] S.T. Nguyen, D. Tan, J.M. Lee, S.W. Chan, J.Y. Wang, X. Wang, International Journal of Hydrogen Energy 36 (2011) 9645–9652.
- [37] C. Xu, Z. Tian, P. Shen, S.P. Jiang, Electrochimica Acta 53 (2008) 2610–2618.
- [38] L.D. Zhu, T.S. Zhao, J.B. Xu, Z.X. Liang, Journal of Power Sources 187 (2009) 80–84.
- [39] R.N. Singh, A. Singh, Anindita, Carbon 47 (2009) 271–278.
- [40] S.T. Nguyen, H.M. Law, H.T. Nguyen, N. Kristian, S. Wang, S.H. Chan, X. Wang, Applied Catalysis B: Environmental 91 (2009) 507–515.
- [41] C. Bock, C. Paquet, M. Couillard, G.A. Botton, B.R. MacDougall, Journal of the American Chemical Society 126 (2004) 8028–8037.
- [42] Y. Suo, I.M. Hsing, Electrochimica Acta 55 (2009) 210–217.
- [43] R.E. Fuentes, B.L. Garcia, J.W. Weidner, Journal of the Electrochemical Society 158 (2011) B461–B466.
- [44] A.S. Attar, M.S. Ghamsari, F. Hajiesmaeilbaigi, S. Mirdamadi, K. Katagiri, K. Koumoto, Journal of Materials Science 43 (2008) 5924–5929.
- [45] J.B. Condron, Surface Area and Porosity Determinations by Physisorption: Measurements and Theory, 1st ed., Elsevier, Amsterdam, 2006.
- [46] Y. Liu, J.M. Szeifert, J.M. Feckl, B. Mandlmeier, J. Rathousky, O. Hayden, D. Fattakhova-Rohlfing, T. Bein, ACS Nano 4 (2010) 5373–5381.
- [47] P.S. Archana, R. Jose, T.M. Jin, C. Vijila, M.M. Yusoff, S. Ramakrishna, Journal of the American Ceramic Society 93 (2010) 4096–4102.
- [48] Y. Wang, B.M. Smarsly, I. Djerdj, Chemistry of Materials 22 (2010) 6624–6631.
- [49] F. Ettingshausen, A. Weidner, S. Zils, A. Wolz, J. Suffner, M. Michel, C. Roth, ECS Transactions 25 (2009) 1883–1892.
- [50] W. Kraus, G. Nolze, Journal of Applied Crystallography 29 (1996) 301–303.
- [51] P.A. Desario, M.E. Graham, R.M. Gelfand, K.A. Gray, Thin Solid Films 519 (2011) 3562–3568.
- [52] D. Morris, Y. Dou, J. Rebane, C.E.J. Mitchell, R.G. Eggleton, D.S.L. Law, A. Vittadini, M. Casarin, Physical Review B: Condensed Matter and Materials Physics 61 (2000) 13445–13457.

- [53] S.B. Zhang, S.H. Wei, A. Zunger, *Physica B: Condensed Matter* 273–274 (1999) 976–980.
- [54] A. Zunger, *Applied Physics Letters* 83 (2003) 57–59.
- [55] B. Babic, J. Gulicovski, L. Gajic-Krstajic, N. Elezovic, V.R. Radmilovic, N.V. Krstajic, L.M. Vracar, *Journal of Power Sources* 193 (2009) 99–106.
- [56] B. Hammer, J.K. Nørskov, *Advances in Catalysis* 45 (2000) 71–129.
- [57] J. Greeley, J.K. Nørskov, M. Mavrikakis, *Annual Review of Physical Chemistry* (2002) 319–348.
- [58] B. Hammer, J.K. Nørskov, *Advances in Catalysis* (2000) 71–129.
- [59] Z.X. Liang, T.S. Zhao, J.B. Xu, L.D. Zhu, *Electrochimica Acta* 54 (2009) 2203–2208.